Self calibration of multiple LIDARs and cameras on autonomous vehicles

Marcelo Pereira[a,d], Vitor Santos[a,c,d,*], Paulo Dias[b,c,d]

[a] *Department of Mechanical Engineering*
[b] *Department of Electronics, Telecommunications and Informatics*
[c] *IEETA-Institute for Electronics Engineering and Informatics of Aveiro*
[d] *University of Aveiro, Portugal*

Abstract

Autonomous navigation is an important field of research and, given the complexity of real world environments, most of the systems rely on a complex perception system combining multiple sensors on board, which reinforces the concern of sensor calibration. Most calibration methods rely on manual or semi-automatic interactive procedures, but reliable fully automatic methods are still missing. However, if some simple objects could be detected and identified automatically by all the sensors from several points of view, then automatic calibration would be possible on the fly. The idea proposed in this paper is to use a ball in motion in front of a set of uncalibrated sensors allowing them to detect its center along the successive positions. This set of centers generates a point cloud per sensor, which, by using segmentation and fitting techniques, allows the calculation of the rigid body transformation between all pairs of sensors. This paper proposes and describes such a method with results demonstrating the validity of the method.

Keywords: Point cloud, 3D data fitting, rigid body transformation

*Corresponding author
Email address: vitor@ua.pt (Vitor Santos)

1. Introduction

Many vehicles with autonomous navigation capabilities, and also many advanced drivers assistance systems, rely on LIDAR (Light Detection And Ranging) and VISION based sensors. Moreover, most of the developed systems use multiple sensors simultaneously, in some cases even combining different types of the same sensors (for example 1D and 2D LIDARs). Thus, when there is more than one sensor in the same setup, a calibration procedure must take place to combine data from different sensors in a common reference frame. In order to solve that necessity, this work presents a new extrinsic calibration method. Differently from the majority of existing methods, which are manual or semi-automatic, the proposed method is fully automatic, with no requirement of manual measurements or manual correspondences in the sensor data-sets. Instead of using those approaches, a ball is used as a calibration target allowing the detection of its center by all sensors and then perform the several registration steps. To estimate the full transformation between the sensors, at least three 3D point correspondences between the sensors are needed, but more than that is used for precision purposes. These points can be estimated during ball motion, which furthermore increases the accuracy of the method as a significant number of points can be obtained during that movement.

1.1. Context of the Work

This work is part of the ATLASCAR project [1], carried out at the University of Aveiro, whose main purpose is the research and development of solutions on autonomous driving and Advanced Driver Assistance System (ADAS). For that goal, and besides an extensive intervention on many fronts, a common Ford Escort car was equipped with a rich set of sensors dedicated mainly to the perception of the surrounding environment (Fig. 1).

Figure 1: AtlasCar, a Ford Escort adapted for autonomous driving capabilities. On the right are sensors used in this work (SICK LMS151 and LD-MRS40001, Point Grey camera and SwissRanger).

The car is equipped with several exteroceptive sensors, namely a stereo camera, a 3D LIDAR, a foveated vision unit and additional planar laser range finders. The planar lasers already installed on the car are two Sick LMS151, and a custom made 3D laser using a Sick LMS200 in a rotating configuration adapted from [2]. Additionally, a new multi-layer laser (sick LD-MRS 400001) and two Point Grey camera are available as well as a SwissRanger 3D TOF used occasionally in some experiments and contexts. The sensors that are part of the study in this paper are illustrated on the right side of Figure 1, and Table 1 presents some of their main characteristics.

1.2. Related Work

Over the past several years, a number of proposed solutions for the calibration between a camera and a laser were introduced, including some automatic on-line calibration solutions as presented in [3]. In [4] a method to estimate the motion of a camera-laser fusion system was developed, by projecting the laser points onto the images using the Kanade-Lucas-Tomasi track [5] and tracking to other frames to be used as 3D-2D correspondences using a three-point method based in the algorithm developed by Bock et al. [6]. In [7] a plane with a printed black ring and a circular perforation is used to solve the extrinsic calibration between a camera and a multi-layer LIDAR; the method consist of estimating

Table 1: Properties of the main LIDAR based sensors onboard the ATLASCAR

	Sick LD-MRS400001	Sick LMS151	SwissRanger sr4000
Scan planes	4, with full vertical aperture of 3.2°	1	
Field of view	2 scan planes: 85° 2 scan planes: 110°	270°	43.6°(h) × 34.6°(v)
Scanning frequency	12.5 Hz/25 Hz/50 Hz	25 Hz/50 Hz	
Angular resolution	0.125°/0.25°/0.5°	0.25°/0.5°	
Operating range	0.5 m - 250 m	0.5 m - 50 m	0.1 m - 5.0 m
Statistical error	± 100 mm	± 12 mm	±10 mm

different poses of the calibration target detected simultaneously by the camera and the multi-layer LIDAR, resulting in a set of point correspondences between frames (circle centers of each pose), that are used to compute the extrinsic calibration by using the singular value decomposition (SVD) along with a the Iterative Closest Point (ICP) algorithm to refine the resulting transformation. A similar approach is used in [8] to calibrate the same set of sensors; a planar triangle plane is used as target to extract correspondences between sensors, and the extrinsic calibration between sensors is solved using the Levenberg-Marquardt algorithm, that projects the laser points into the image. There are also some other studies for the specific problem of calibration between LIDAR sensors, however, there is still room for improvement since no fully automatic method using perception sensor information and adapted to any configuration is already available. Previous works on the ATLASCAR project used a technique that also uses a calibration target, but it requires manual input from the user[9]. Other authors developed algorithms to calibrate one [10] or two [11] single-beam LIDARs within the body frame; both methods use approaches that rely on establishing feature correspondences between the individual observations by preparing the environment with laser-reflective tape, which additionally requires an intensity threshold for correspondences and some initial parameters. A more recent method [12] is based on the observation of perpendicular planes;

this calibration process is constrained by imposing co-planarity and perpendicularity constrains on the line segments extracted by the different laser scanners; despite being an automatic calibration method, it also requires some initial conditions, and does not provide the versatility of the method presented in this paper. Finally an approach using a sphere target to perform extrinsic calibration of multiple 3D cameras was presented in [13]. This work presents some similarities with the proposal of the paper since the user moves the target around the workspace, moving it to different positions and heights within a shared viewing area, and the algorithm automatically detects the center of the ball in the data from each camera, and then uses those centers as corresponding points to estimate the relative positions of the 3D sensors. However, that approach was used only with Kinect sensors with a smaller ball and a reduced working range.

2. Proposed solution

The proposed solution is to estimate the rigid body transform between three different sensors using a ball as calibration target. The only restriction of the calibration target is about its size (diameter). The size of the calibration target is related to the angular resolution of the sensors used; after some empirical experiments, it was concluded that the ball must have a diameter large enough for the sensors to have at least 8 measurements on the target at 5 m.

The approach used to obtain the calibration between all the devices is achieved in three stages. First, each sensor must detect the center of the ball; then, the ball is placed in motion in front of the sensors allowing them to detect its center along successive positions, creating at the same time a point cloud for each of them. The condition to consider a new reference point (ball center) for each point cloud is that each new point (ball center) is separated from the previous one by some minimum distance. Finally, one sensor is chosen as reference and the remainder are calibrated relatively to it one at a time by using an algorithm available on the Point Cloud Library (PCL) [14].

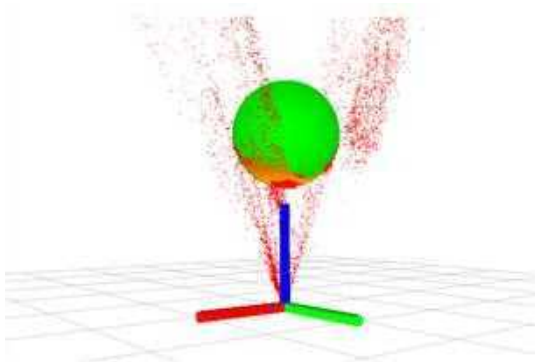

Figure 2: Detection in a Swissranger cloud of points.

3. Ball detection algorithms

The method to find the center of the ball depends on the type of data. In the following sections are described the methods used for the ball detection in the different sensors.

3.1. Sphere center detection in 3D data: SwissRanger

The ball recognition in the SwissRanger is achieved using the PCL segmentation capabilities, namely the sample consensus module. The Random Sample Consensus (RANSAC) [15] is the algorithm applied in the point cloud from the SwissRanger, which is an iterative method used to estimate parameters of a mathematical model from a set of data containing outliers. In this case, the model is a sphere, so the resulting parameters are the coordinates of the center of the ball and its radius. Figure 2 shows the application of the RANSAC algorithm on the ball detection.

3.2. Sphere center detection on LIDAR lasers

The method for 2D data is based in finding circular arcs, taking advantage of the particularity that any planar section of the ball is a circle. Thus, the process to detect the center of the ball is divided in the following sequence: segmentation of the laser scan, detection of circle and calculation of its properties

(center coordinates and radius), and calculation of the center of the ball given the properties of the target (diameter).

It is important to mention that in 2D scans, due to the symmetry of the ball, there is an ambiguity relatively to which of the hemispheres belongs the detected circle, since every section of the ball has a symmetric section relatively to the hemisphere, which gives two solutions for the center of the ball (one above and another below the detected section). Consequently, some a priori information about the position of the sensor relatively to the ball is required. For the Sick LD-MRS, the idea was to solve this problem taking advantage of its multi-layer technology, however, due its associated error, it turned out to be not possible. After some tests with the Sick LD-MRS, when all the laser scans were on the lower ball hemisphere, the lowest scan should give the smallest circle diameter (since it is the smallest section of the ball), however, due its error, that was not always verified. Thus, also some a priori information about the relative placement of this sensor may be required.

3.2.1. Segmentation

Segmentation is a very important part before the calibration process. The main goal is to cluster the point cloud in sub sets of points which have high probability to belong to the same object through detected discontinuities in the laser data sequence, which are called break-points.

Several method are available to perform 2D point cloud segmentation. Based on the work of Coimbra [16], the Spatial Nearest Neighbour (SNN) was used since it appears to be the most consistent over different tested scenes.

The SNN is a recursive algorithm where the distance between a scanned point and all the other points that are not yet assigned to a cluster is computed. If that distance is smaller than a certain threshold the points are assigned to that cluster. Figure 3 shows the result of the segmentation in a scan and the cluster related to the ball. The only variable in this algorithm is the threshold value D_{th} , so it is expected that for a higher D_{th} the result will be larger clusters, and for a smaller D_{th} the result will be smaller clusters.

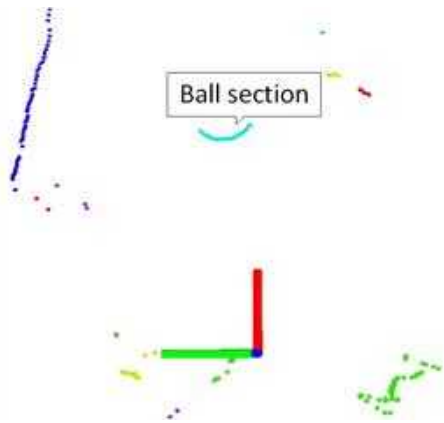

Figure 3: Result of the segmentation on sensor Sick LMS151.

3.2.2. Circle Detection

The method used for circle detection is inspired on a work developed for line, arc/circle and leg detection from laser scan data [17]. The circle detection makes use of a technique named Internal Angle Variance (IAV). This technique uses the trigonometric properties of the arcs: every point in an arc has congruent angles (angles that have the same amplitude) in respect to the extremes. This property can be verified in Figure 4. Let P_1 and P_4 be the extremes of the arc, and P_2 and P_3 random points belonging to the same arc. Then $\angle P_1P_2P_4 = \angle P_1P_3P_4$ because both angles measure one-half of $\angle P_1OP_4$.

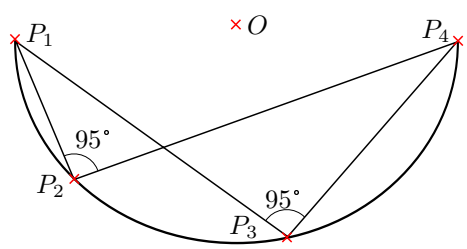

Figure 4: Congruent angles of points on an arc in respect to the extremes.

The detection of circles involves calculating the mean of the aperture angle ($\bar{m}$) between the extreme points and the remainder points of a cluster, as well as the standard deviation (σ). In an earlier approach, and considering that the

scan covers approximately half a circle, values of standard deviation smaller than 8.6° and values of mean aperture between 90° and 135° were used to define a positive detection. However, those values are dependent of two factors: the error associated to the sensors, and how much of the circle is covered by the scan. Thus, after analyzing the results empirically, the values were adjusted to standard deviations under 5°, and values of mean aperture between 105° and 138° for the sick LMS151, and 10° and between 110° and 135°, respectively for the sick LD-MRS400001. These adjustments allowed to obtain the best results avoiding the detection of false circles. Considering that a segment S has n points (P), say $S = \{P_1, P_2, ..., P_n\}$, the mean and standard deviation of the angle are calculated as follows: $\bar{m} = \frac{1}{n-2}\sum_{i=2}^{n-1} \angle P_1 P_i P_n$ and $\sigma = \sqrt{\frac{1}{n-2}\sum_{i=2}^{n-1} \left(\angle P_1 P_i P_n - \bar{m}\right)^2}$.

3.2.3. Calculation of the circle properties

The calculation of the center and radius of the circle uses the method of least squares to find the circle that best fits the points. Given a finite set of points in $\mathbb{R}^2$, say $\{(x_i, y_i)|0 \leq i < N\}$, first calculate their mean values by $\bar{x} = \frac{1}{N}\sum_i x_i$ and $\bar{y} = \frac{1}{N}\sum_i y_i$. Let $u_i = x_i - \bar{x}$, $v_i = y_i - \bar{y}$ for $0 \leq i < N$, and defining $S_u = \sum_i u_i$, $S_{uu} = \sum_i u_i^2$, $S_{uv} = \sum_i u_i v_i$, etc. The problem is to solve first in (u, v) coordinates, and then transform back to (x, y).

Considering that the circle has center (u_c,v_c) and radius R, the main goal is to minimize $S = \sum_i g(u_i, v_i)^2$, where $g(u, v) = (u - u_c)^2 + (v - v_c)^2 - \alpha$, and $\alpha = R^2$. To do that, it is necessary to differentiate $S(\alpha, u_c, v_c)$ in order to the two variables, resulting in the following expressions:

$$u_c S_{uu} + v_c S_{uv} = \frac{1}{2}(S_{uuu} + S_{uvv}) \tag{1}$$

and

$$u_c S_{uv} + v_c S_{vv} = \frac{1}{2}(S_{vvv} + S_{vuu}). \tag{2}$$

Solving expressions (1) and (2) simultaneously allows to obtain (u_c, v_c). Then, the center (x_c, y_c) of the circle in the original coordinate system can be obtained as: $(x_c, y_c) = (u_c, v_c) + (\bar{x}, \bar{y})$, being $\alpha = u_c^2 + v_c^2 + \frac{S_{uu}+S_{vv}}{N}$. The result of the

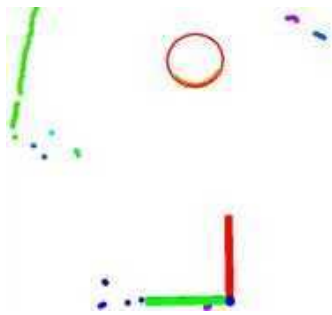

Figure 5: Result of the circle detection in real data from the sensor Sick LMS151.

combination of circle detection with the properties of the circle is illustrated in Figure 5.

3.2.4. Calculation of the center of the ball

After knowing all the properties of the circle, it is possible to calculate the center of the ball through trigonometric relations as shown in Figure 6, where R is the radius of the ball, R' the radius of the circle and d the distance between the center of the circle and the center of the ball, with $d = \sqrt{R^2 - R'^2}$. Taking into account the ambiguity for the 2D lasers mentioned in subsection 3.2, and considering that the center of the circle has (x_c,y_c) coordinates, the coordinates of the center of the ball for this laser are defined as follows: $(X_c, Y_c, Z_c) = (x_c, y_c, \pm d)$. Figure 7 illustrates an example of the ball detection in a 2D scan.

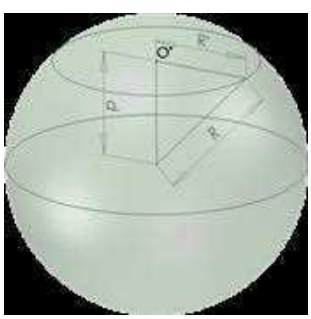

Figure 6: Example of the cross-section of the sphere at a distance d from the sphere's center.

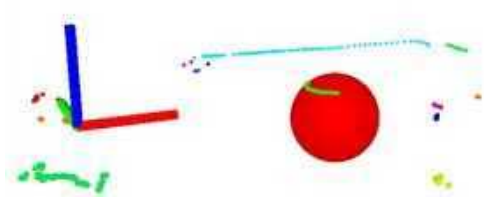

Figure 7: Detection of the ball in a 2D scan from the Sick LMS151.

In order to simplify the calculations in the 3D multi-layer laser, the coordinates of the circle center are transformed into the XY plane for each layer; then for each layer, the center of the ball is calculated in the same way as in the 2D laser. After this, the centers of the ball are transformed back into the respective original plane.

At this point, for each layer, the center of the ball was calculated, which means that there are as many centers as layers. Thus, statistically, the center of the ball is obtained by calculating the mean of all the centers. Considering that there are n layers and the different circles have $(x_{c_1}, y_{c_1}, z_{c_1}; ...; x_{c_n}, y_{c_n}, z_{c_n})$ coordinates, the center mean coordinates are defined as follows: $(X_c, Y_c, Z_c) = (\frac{1}{n}\sum_{i=1}^{n} x_{c_i}, \frac{1}{n}\sum_{i=1}^{n} y_{c_i}, \frac{1}{n}\sum_{i=1}^{n} z_{c_i})$. In the present case we have $n = 4$.

3.3. Sphere center detection on cameras

Giving continuity to the work presented in [22], the integration of the cameras on the calibration process was also addressed. The first approach to detect the ball was the Hough Transform, available on the OpenCV library. The Hough Transform is a method used to extract features of specific shapes in images. Since the calibration target is a ball, the Hough Circle Transform was used to find, in the image, points of a circle that best fit the ball, returning its parameters (apparent radius in pixels $R_{pix} = D_{pix}/2$, and center in pixels $(x_{c_{pix}}, y_{c_{pix}})$). Assuming that the intrinsic parameters of the camera are known (obtained previously by a traditional calibration method), as well as the ball physical diameter ($D = 2R$), it is possible to determine the center of the ball in the camera coordinate system.

Discarding the camera roll angle (i.e, the horizontal coordinate axis of camera is considered also to be the horizontal axis of the real world), there remains to detect the distance to the ball center (Z_c), the pitch angle (rotation around camera x axis, ψ) and the yaw angle (rotation around camera y axis, θ). Since we know the real ball diameter (D) and the apparent diameter in pixels on image (D_{pix}), it is possible, by using the intrinsics, to determine the distance to the ball. With the coordinates in pixels of the center of the ball, and knowing

already its distance, by using once again the intrinsics, it is possible to calculate the pitch and yaw angles, completing the detection of the ball center coordinates from the camera coordinate frame (X_c, Y_c, Z_c). A complete demonstration of this procedure can be seen, for example, in [23].

The problem we face was related to the ball used in these experiments that was not fully suited, mainly outdoors, to be not fully suited to confirm results because its color and texture does not make it easy to detect its contour in a reliable way. One of the causes is the reflections in the white parts. Another texture on the ball should be used to assess the method, and that will be work for future developments. So, this approach of ball detection in the image was discarded at this stage.

However, in order to try a real integration of cameras and lasers on the same setup, an alternative solution was explored by using a stereo rig to obtain a cloud of points of the scene and detect the ball using the same algorithm used for the SwissRanger (see section 3.1), which was also performed using algorithms present in OpenCV.

3.3.1. Stereo procedures

The use of a stereo system consists of four main steps: perform a stereo calibration; compute the disparity map; perform a 3D reconstruction based on the disparity map and create a point cloud; finally, apply the same method used for the SwissRanger.

Stereo calibration is the process of computing the geometric relationship between the two cameras in space. For the calibration of a single camera, OpenCV uses the method described by Zhang in [24] to estimate the intrinsic matrix of the camera. This process is executed on stereo calibration for the two cameras, and then, the information taken by both cameras during the process is related to compute the extrinsic parameters between cameras. The result of the stereo calibration is used to perform the rectification, with the main goal of re-project the image planes of the two cameras so they reside in the exact same plane, with image rows perfectly aligned into a frontal parallel configuration. The

(a) Image camera 1. (b) Image camera 2.

Figure 8: Images of a scenario taken by both cameras.

algorithm provided by OpenCV already makes the undistortion and rectification of the images, since they are related. OpenCV implements two methods to compute the rectification: Hartley's algorithm [25] and Bouguet's algorithm. Bouguet's algorithm was the chosen. For more information, this algorithm is a completion and simplification of the method first presented by Tsai [26] and Zhang [27, 24].

The stereo correspondences consists of matching 3D points of the same scene in the two different camera views, which can be computed only over the visual areas in which the views of the two cameras overlap. The regions in one image which have no counterparts in the other image, are referred to as occlusions. This is the reason why better results are obtained if the arrangement of the cameras are the the closest possible to near frontal parallel. In OpenCV there are two different algorithms to calculate correspondences: the block-matching (BM), which is similar to the one developed by Kurt Konolige [28], and an adaptation of Hirschmuller's semi-global matching (SGM) [29], referred as the semi-global block matching (SGBM). After some tests it was concluded that the SGBM presents better results than the BM algorithm, and it is possible to observe that the SGBM exhibits a smoother disparity image, and with less noise, than the BM algorithm. To illustrate the differences between the two methods, Figure 8 shows the images taken by both cameras, and Figure 9 shows the resulting disparity image by both algorithms.

Knowing the geometric arrangement obtained from the stereo calibration, it

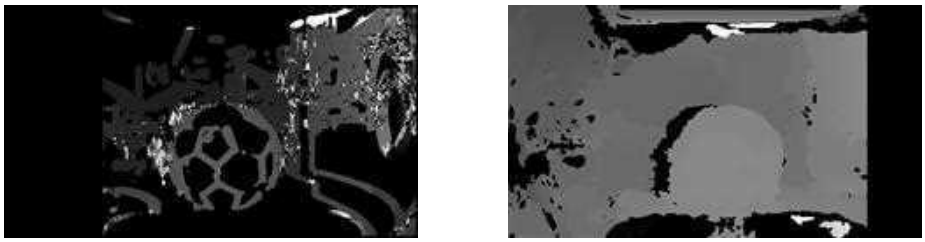

(a) BM. (b) SGBM.

Figure 9: Disparity images of BM and SGBM algorithms.

is possible re-project the disparity map into depth by triangulation.

After performing the 3D reconstruction of the disparity map into a point cloud, the ball center detection is performed as described on subsection 3.1. Figure 10 shows an example of the disparity map re-projection into 3D coordinates on the left, and the detection of the ball on the right.

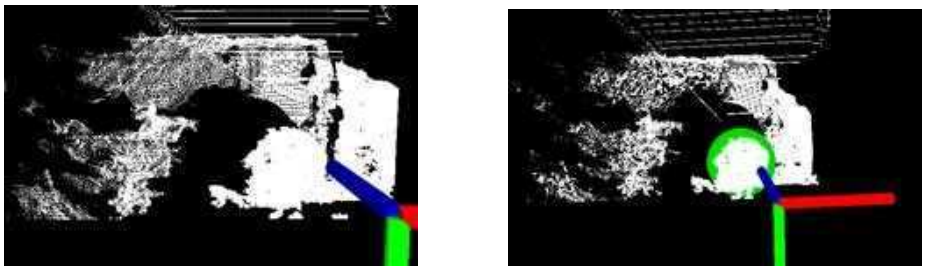

(a) 3D reconstruction. (b) Ball detection.

Figure 10: 3D reconstruction of the disparity map and ball detection.

4. Calibration

The 3D transformation between the cloud of points generated from the ball centers in each sensor are estimated using an Absolute Orientation algorithm. The implementation used is available in PCL, which is based on the Singular Value Decomposition (SVD) method proposed in [18, 19].

5. Software Architecture

The entire methodology has been implemented in C++ under the ROS platform. ROS [20] is a development environment specifically for applications in robotics, usually used in large projects that, due to its modular architecture, allows to reduce projects complexity using smaller modules with specific applications. Also, those modules can be used for other applications and not only in a single project. Figure 11 shows all the processes that run during the calibration and what each of them is publishing and subscribing. Four processes are shown (one for each sensor), but this is scalable for more sensors.

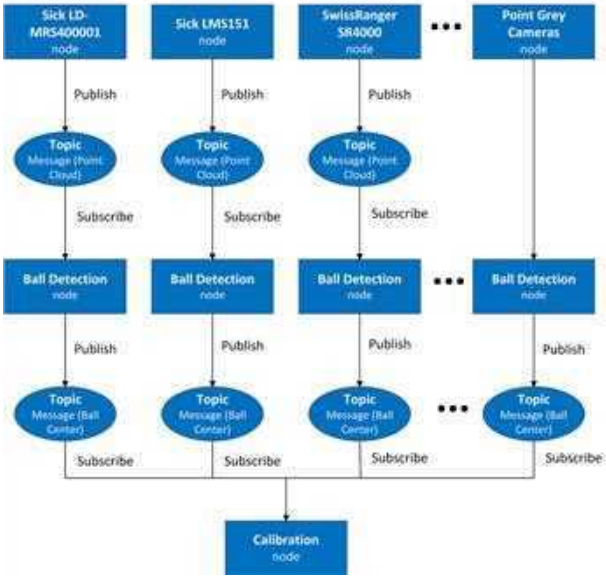

Figure 11: Calibration process scheme.

6. Results

Several experiments were carried out and results are focused in the following three fronts: i) evaluating the consistency in the ball detection in each sensor; ii) the consistency in the 3D transformation estimation depending on the number of points used; and iii) the global validation of the method. The experiments

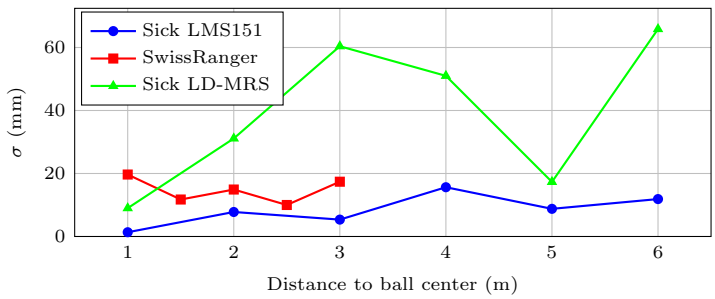

Figure 12: Standard deviation of ball center detection for several distances.

carried out do not provide an absolute validation of the procedure since no ground-truth is available but, nevertheless, the obtained results demonstrate the validity of the method.

6.1. Consistency of ball detection

In the ball detection test, and in similar conditions, the ball was placed statically at different distances from the sensors and, for each position, 500 samples of coordinates of the ball center were acquired. From these samples, a mean and a standard deviation were calculated. Figure 12 shows the standard deviations of the measurements of the three sensors used on this test.

The results show that the variation is consistent with the error associated to each sensor as shown in Table 1 (below 10 cm for the Sick LD-MRS, and about 1 cm for the remaining sensors). In the case of the SwissRanger a greater variation is verified for the closest and furthest distances; it may be due to the proximity of the ball and a lower density of points for further distances, but this is only a belief that needs a more detailed study for confirmation. Nonetheless, the standard deviation in the detection of the ball is not larger than the error associated to the standalone sensors, indicating that the method does not introduce new measurement errors. For the Sick LD-MRS, even with results in accordance with its associated error, it is difficult to evaluate the interference of the distance of the ball on its detection, which can be possibly explained by the fluctuations in the data provided by the sensor; for example, it

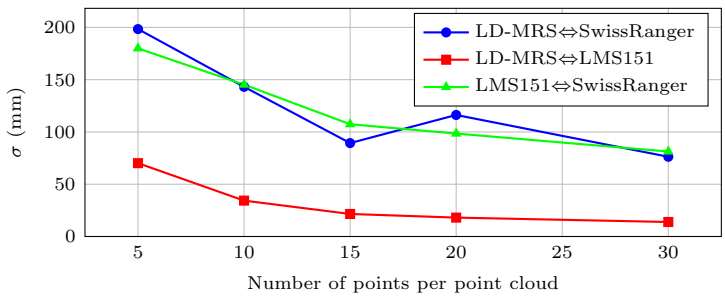

Figure 13: Standard deviation of the translation between the three sensor pairs.

is possible to have a set of 500 measurements of a static object at 10 m, where 80% of the measurements have a deviation of ±0.01 m and the remainder 20% have a deviation of ±0.08 m. On the other hand, for the exact same conditions, if a new set of 500 measurements is obtained, a ratio of 50%/50% may be found instead.

6.2. Consistency of the geometric transformation

In the second set of tests, a calibration between all the sensors was performed using always the same setup; this was done by using different sizes of the point clouds (number of points), where each point of the cloud corresponds to a different position of the ball along its motion in front of the sensors. Thus, for each size of the point clouds, a set of 20 calibrations was performed with the respective matrix of the estimated rigid transformation. The analysis of results compares the translation and rotation; the translation is obtained directly from the matrix of rigid associated geometric transformation; considering the rotation matrix (R) from calibration and R_x, R_y and R_z the generic rotations around each axis, R is defined as $R = R_x(Roll)R_y(Pitch)R_z(Yaw)$, which allows to be solved and obtain the Euler angles ($Roll$, $Pitch$, Yaw). Then, as in the first test, a mean and a standard deviation of the translation and Euler angles are calculated, with the difference that the Euler angles are analyzed individually. Figure 13 shows the results for the translation, and Figure 14 presents the results for the Euler angles.

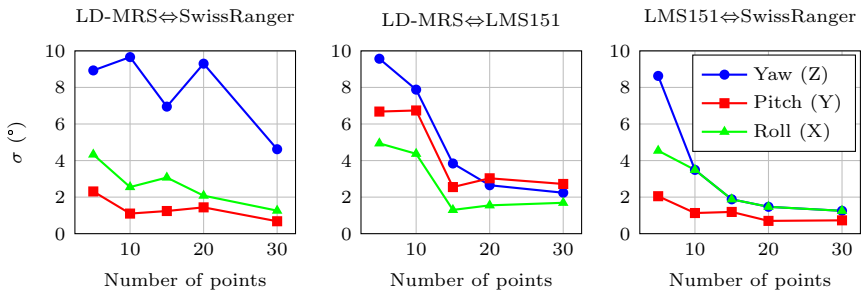

Figure 14: Standard deviation of the Euler angles between the three sensor pairs.

Figure 15 shows the setup used for the calibration and the estimated positions of the sensors after being calibrated. As expected, the standard deviation decreases with the number of points, and stabilizes at around 20 points; for this test the minimum distance between consecutive points was 10 cm. The mean variation from point clouds of 20 points is lower than 10 cm and about 4˚or 5˚, which, once again, is in the range of the standalone sensors errors.

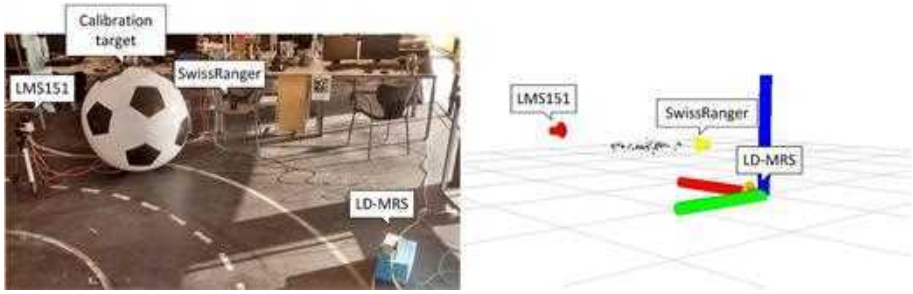

Figure 15: Layout of the sensors on then scene and positions detected by the calibration process.

6.3. Validation of the method

The difficulty of having a ground-truth makes complicated the absolute validation of the method, which would allow the comparison of the estimated transformation with the exact transformation among sensors. It is very difficult to guarantee with precision if the obtained calibration is correct, given the difficulty to measure exactly the correct pose between pairs of sensors. This problem

is particularly difficult with rotations (it is possible to have a fairly reasonable evaluation of the translation with simple measurements with a measuring tape), which is critical, since small errors in rotation may result in large error in the final registered data.

With this problem in mind, our goal has been to perform a calibration of all the devices with respect to the sensor with better accuracy. Then, the point cloud of the reference sensor is used as ground-truth, and on the remainder sensors is applied the resulting transformation from the calibration. This allows to evaluate how well the point clouds fit in the reference point cloud by calculating the absolute mean error and the standard deviation of the corresponding points.

This test was performed in a real full size vehicle (AtlasCar) to evaluate the method on real conditions. And since these tests took place outdoors, the devices used are the ones that will have some functionality on the AtlasCar project, which means that the set of sensors does not include the SwissRanger. The main reason to exclude the SwissRanger is that the sensor does not work well outdoors because it is affected by sunlight that interferes with the infrared light projected by the system.

The sensors used in this experiment are: the Sick LD-MRS, the two Sick LMS151 and the stereo system. One of the Sick LMS151 was chosen as reference (henceforth named Sick LMS151(A)) and the remainder are calibrated relatively to it. The experience has the following steps:

- Chose one of the sensors as reference (in this case the Sick LMS151(A) was chosen given that this is the sensor with better accuracy);
- Perform the point cloud acquisition for each sensor and calibrate them with respect to the reference sensor;
- Apply the resulting transformation on the point clouds of the calibrated sensors;
- Calculate the error of each point belonging to the point cloud of the calibrated sensors relatively to the corresponding points of the ground-truth

Figure 16: Setup used on the validation test and the sensor positions.

(point cloud of the reference sensor);

- Calculate the mean error and standard deviation of the previous step.

The acquisition of the point clouds were performed with two different approaches: i) following approximately a grid-pattern ii) acquire random points during the motion of the ball in front of the sensors. The idea of acquiring a pattern was to perform a study about the influence of the distribution of the points on the calibration by selecting different points from the pattern. The acquisition of random points is to evaluate the calibration method in a normal situation. Figure 16 shows the setup mounted on AtlasCar, where can be seen that the Sick LD-MRS is placed on the top of a box because there is not yet a support to apply it in the car, nonetheless, its final location will not be much different from where it was placed.

6.3.1. Calibration with a pattern of acquisition spots

To perform the acquisition with the ball moving along a grid/pattern, several markers were positioned on the floor and the ball was placed as close as possible to each marked position. In each of the acquisition spots, a point cloud was acquired for each sensor. Also, the resulting point clouds of each sensor were divided in two subsets of points: one with the central points of the point cloud, which will be called inner points, and the other with the remainder points, which will be called outer points. These two different subsets were used to evaluate the influence of the range and distribution of the acquisition spots on

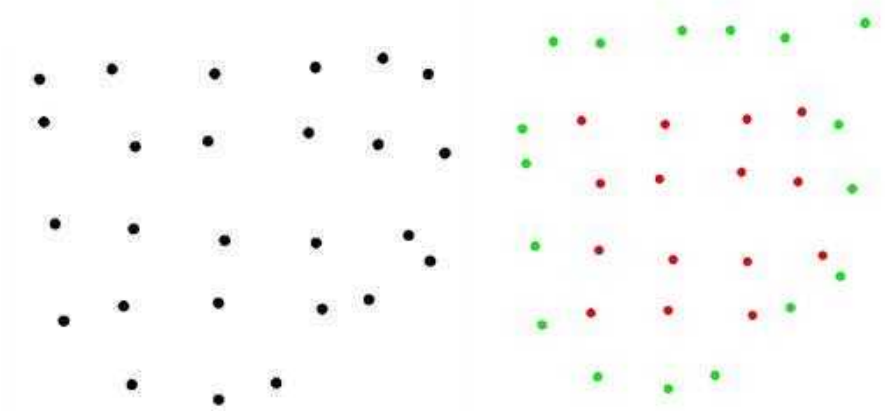

(a) Point cloud of ball centers. (b) The two subsets of ball centers.

Figure 17: Resulting point cloud of successive ball centers on the Sick LMS151 sensor, and the two selected sub set of points on it. The inner points are in red and the outer points in green.

the transformation estimation. Figure 17 shows on the left the resulting point cloud for the Sick LMS151, and on the right the selected inner points in red and the outer points in green.

Figure 18 shows the point clouds of each sensor with respect to their own frame. On the left the point clouds with the inner points and on the right the point clouds with the outer points.

The calibration of the sensors with respect to the reference on both cases (with the inner and outer points) is performed. Then, the resulting transformation was applied on the point cloud of each sensor. To evaluate the quality of the calibration, the distance between each corresponding point of the calibrated sensors to the reference sensor was calculated. The measurements obtained were the standard deviation and the error associated to each corresponding point. Then, the absolute mean error is calculated for each calibrated sensor. The resulting standard deviation and the absolute mean error of the calibration using the inner points are shown on Table 2, and using the outer points on Table 3.

In order to have a better idea of the quality of the calibration, the sensors

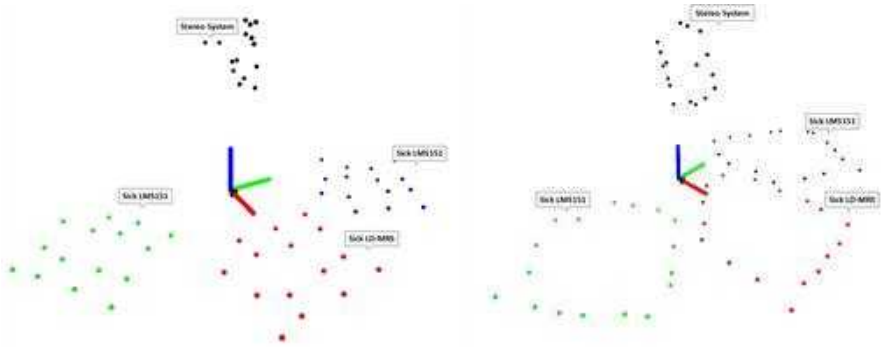

(a) Inner points. (b) Outer points.

Figure 18: Representation of the sensors point clouds of several ball centers on their own coordinate system. On the left the inner points (15 centers of the ball), and on the right the outer points (17 centers of the ball).

Table 2: Standard deviation and absolute mean error for each sensor calibration against Sick LMS151(A) using the inner points.

	Standard deviation [cm]	Absolute mean error [cm]
Sick LMS151(B)	2.90	2.29
Sick LD-MRS	3.76	3.24
Stereo system	38.47	31.34

Table 3: Standard deviation and absolute mean error for each sensor calibration against Sick LMS151(A) using the outer points.

	Standard deviation [cm]	Absolute mean error [cm]
Sick LMS151(B)	3.80	2.62
Sick LD-MRS	4.54	3.73
Stereo system	76.09	63.57

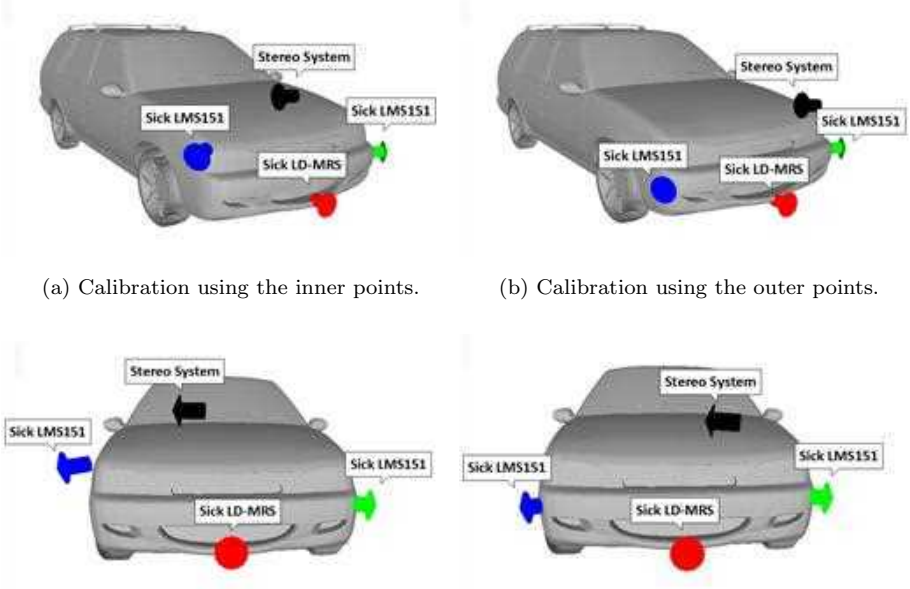

(a) Calibration using the inner points.

(b) Calibration using the outer points.

(c) Calibration using the inner points.

(d) Calibration using the outer points.

Figure 19: Calculated placement of the sensors in a CAD model of the AtlasCar using calibration with the two point subsets.

were placed on a CAD model of the AtlasCar. The result is shown on Figure 19, where the sensors are represented by arrows pointing in the X axis direction of their own referential system.

On Figure 18 it is clear that the stereo system is not very reliable. This can be due to several factors, from a bad calibration of the stereo system to the scene where the pattern was acquired, which has a lot of close objects that may interfere on the ball detection. Also, due to the reflection of light on the ball and its large areas with uniform color, the disparity map shows some noise that affects the re-projection of the ball to 3D coordinates. The re-projection of the ball instead of being a perfect spherical surface, presents an irregular spherical surface, and sometimes is hard to detect as being part of the ball.

As consequence of the bad pattern acquisition by the stereo system, its calibration presents a big standard deviation and absolute mean error for both

calibrations as presented on Table 2 and 3.

By analyzing the lasers' calibration on Table 2 and 3, the results between both calibrations does not differ much. The standard deviation and the absolute mean error values are slightly bigger on the outer points, which is related with the furthest measurements of the ball center; however, the difference is so small that it becomes irrelevant. It is interesting to notice that lower errors does not mean a better calibration. Looking at Figure 19, and comparing with the setup used (Figure 16), the displacement of the lasers on the car model seems to be better on the calibration with the outer points. This result was expected, since the more spread the points used for calibration are, the better the results are expected (if all acquisition spots are located in a small region, the errors due to shorter spacing will have a larger influence on the final transformation evaluation).

6.3.2. Calibration with random acquisition spots

The calibration method does not need to follow any particular pattern with the corresponding points. Thus, this test is to evaluate a calibration using points in random positions. Differently from the previous test, this one was realized in an open area without close objects that may interfere on the ball detection. Based on the results obtained in the previous tests about the influence of the number of points on the transformation estimation, we chose a number of 25 corresponding points per point cloud. The resulting point clouds of the calibration process for each sensor with respect to their own frame are shown on Figure 20.

Again, the calibration of the sensors was computed with respect to the one of them taken as reference (the Sick LMS151), and the transformation estimation was applied on the corresponding point cloud. Then, as in the previous test, the position of the sensors after calibration are placed on the car model. The arrangement is shown on Figure 21 along with the real setup for comparison.

Figure 21 shows that the obtained calibration and the real setup appear to be fairly consistent for the lasers. Although the same is not verified for stereo

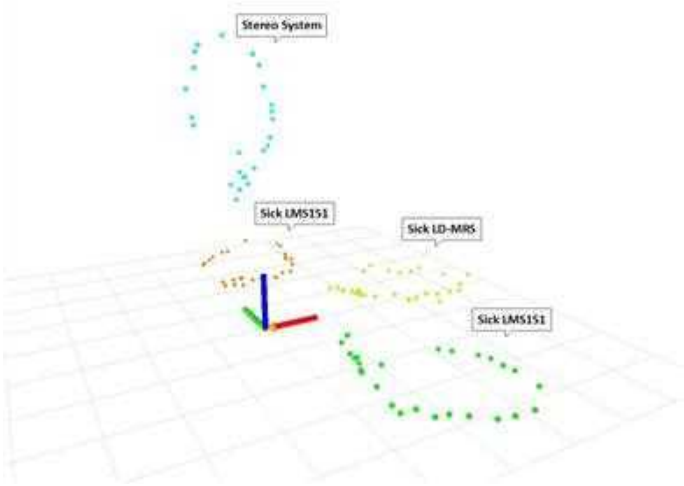

Figure 20: Resulting point clouds for each sensor (yet uncalibrated).

(a) Sensors setup on the AtlasCar.

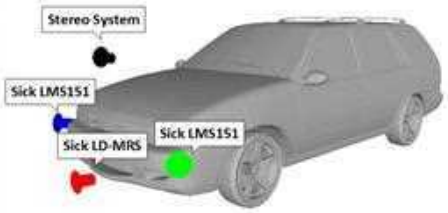

(b) Sensors positions on the car model after the calibration.

Figure 21: Position and orientation of the sensors on the AtlasCar and the car model after the calibration for comparison.

Table 4: Standard deviation and absolute mean error of each calibrated sensor against Sick LMS151(A).

	standard deviation [cm]	absolute mean error [cm]
Sick LMS151(B)	3.11	2.37
Sick LD-MRS	5.99	4.16
Stereo system	21.49	18.19

system; the problem seems to be in the 3D stereo reconstruction process, since the whole 3D cloud of points appears too close to the car. This might indicate problems in the stereo rig calibration.

The evaluation of the calibration was performed exactly as in the previous test. The standard deviation and the absolute mean error for each calibrated sensor is presented on Table 4. The results for the standard deviation and the absolute mean error between lasers is similar to the ones obtained on the previous test. However, the calibration of the stereo system improved significantly. This may be related to the change of scenery where the calibration was performed, since in this scenario close objects that may interfere on the ball detection did not exist. The error is still too large to allow a real use of the stereo system, and further work on the topic is necessary to better understand the causes of this large error and improve the process.

The small error and standard deviation associated between the two lasers Sick LMS151 was expected, since they are the devices with smaller error ($\pm 1cm$), however, the result between the laser Sick LMS151 and the Sick LD-MRS was surprising, since the calibration error is smaller than the error associated to the Sick LD-MRS ($\pm 10cm$). These results prove that the method for the ball detection on the Sick laser does not induce more error than its associated intrinsic error. Also, since the calibration algorithm uses several points and minimizes the sum of the point pairs error, a point with larger error does not affect much the calibration result.

The largest error on the stereo, once again, may be related to reasons pointed

previously, such as the poor image due to the reflection of light on the ball, and its big areas with uniform color.

7. Conclusions and Future Work

This paper proposes a new automatic calibration process to seamlessly calibrate different 2D/3D sensors and cameras by using a ball as calibration target. In the current version, the only a priori parameter required is the relative position of the 2D sensor concerning the ball (whether it is placed above or below the equator).

The good results on the consistency tests for the ball detection and transformation estimation were confirmed with the validation tests by the small errors that were obtained on the calibration of the LIDAR lasers. However, the stereo system presented some limitations on the ball detection, having consequences on the accuracy of its calibration.

Future work involves a detailed study about the integrated calibration of cameras. The achieved integrated camera calibration is a good start, but some improvements must be carried out. For better ball detection with vision, it is advisable the use a ball with more adequate color/texture.

It is also planned to impose full 3D motion paths on the ball, possibly hopping or bouncing in the sensors fields, to solve all ambiguities for any positions of the sensors, and thus requiring no a priori information on hemisphere relative position. This will require a more elaborate algorithm since tracking will be needed to follow the ball and disambiguate its 3D position automatically.

Also, it would be interesting to use external high precision devices (for example a motion capture setup) for a better validation of the method. Finally, in order to simplify the use of the method, an interface is to be developed to be a more user friendly method, including possibly a software package to make available for the ROS community.

References

[1] Santos, V., Almeida, J., Avila, E., Gameiro, D., Oliveira, M., Pascoal, R., Sabino, R., Stein, P.: "ATLASCAR - Technologies for a computer assisted driving system on board a common automobile". In: 13th International IEEE Conference on Intelligent Transportation Systems (ITSC2010). Madeira Island, Portugal. (2010)

[2] J. Dias: Distanciómetro 3D baseado numa unidade laser 2D em movimento contínuo. Masters' thesis, Universidade de Aveiro (2009) [http://hdl.handle.net/10773/2501].

[3] J. Levinson, S. Thrun: Automatic Online Calibration of Cameras and Lasers. In Robotics: Science and Systems (RSS), 2013.

[4] Y. Bok, D. Choi and I. Kweon: Generalized laser three-point algorithm for motion estimation of camera-laser fusion system. In IEEE International Conference on Robotics and Automation (ICRA), pp. 2880-2887, 2013.

[5] J. Shi and C. Tomasi: Good Features to Track. In Proceedings of the IEEE Computer Society Conference on Computer Vision and Pattern Recognition, 1994, pp. 593-600.

[6] Y. Bok, D.-G. Choi, Y. Jeong and I. S. Kweon: Capturing Citylevel Scenes with a Synchronized Camera-Laser Fusion Sensor: In Proceedings of the IEEE/RSf International Conference on Intelligent Robots and Systems, 2011, pp. 4436-4441.

[7] S. A. Rodriguez F., V. Fremont and P. Bonnifait: Extrinsic calibration between a multi-layer lidar and a camera. In IEEE International Conference on Multisensor Fusion and Integration for Intelligent Systems, pp. 214-219, 2008.

[8] S. Debattisti, L. Mazzei, M. Panciroli: Automated Extrinsic Laser and Camera Inter-Calibration Using Triangular Targets. In IEEE Intelligent Vehicles Symposium (IV), pp. 696-701, 2013.

[9] Almeida, M., Dias, P., Oliveira, M., Santos, V.: 3D-2D Laser Range Finder calibration using a conic based geometry shape. In: Image Analysis and Recognition. Ed. by Aurélio Campilho and Mohamed Kamel. Springer Verlag, pp. 312–319 (2012).

[10] J. Underwood, A. Hill, and S. Scheding: Calibration of range sensor pose on mobile platforms. In IEEE/RSJ International Conference on Intelligent Robots and Systems, pp. 3866-3871, 2007.

[11] G. Chao and J. Spletzer: On-Line Calibration of Multiple LIDARs on a Mobile Vehicle Platform. In IEEE International Conference on Robotics and Automation (ICRA), pp. 279-284, 2010.

[12] E. Fernandez-Moral, J. Gonzalez-Jiménez and V. Arévalo: Extrinsic calibration of 2D laser rangefinders from perpendicular plane observations. In The International Journal of Robotics Research, 2015.

[13] M. Ruan and D. Huber: Extrinsic Calibration of 3D Sensors Using a Spherical Target. In Second International Conference on 3D Vision (3DV), pp. 187-193, 2014.

[14] Rusu, R. B., Cousins, S.: 3D is here: Point Cloud Library (PCL). In IEEE International Conference on Robotics and Automation (ICRA), pp. 1-4, 2011.

[15] M. A. Fischler and R. C. Bolles. Random sample consensus: a paradigm for model fitting with applications to image analysis and automated cartography. Commun. ACM, 24(6):381–395, June 1981

[16] Coimbra, D.: LIDAR Target Detection and Segmentation in Road Environment. Masters' thesis, Universidade de Aveiro (2013) [http://hdl.handle.net/10773/11774].

[17] J. Xavier, M. Pacheco, D. Castro and A. Ruano: Fast line, arc/circle and leg detection from laser scan data in a Player driver. In Proceedings of the

2005 IEEE International Conference on Robotics and Automation (ICRA), pp. 3930-3935, 2005.

[18] K. S. Arun, T. S. Huang, and S. D. Blostein: Least-squares fitting of two 3-D point sets. In IEEE Transactions on Pattern Analysis and Machine Intelligence (PAMI), vol. 9, no. 5, pp. 698–700, 1987

[19] B. K. P. Horn: Closed-form solution of absolute orientation using unit quaternions. In Journal of the Optical Society of America A, vol. 4, no. 4, pp. 629–642, 1987.

[20] Quigley, M., Berger, E., A. Y. Ng.: "STAIR: Hardware and Software Architecture". In AAAI 2007 Robotics Workshop, 2007.

[21] G. Bradski and A. Kaehler: Learning OpenCV: Computer Vision with the OpenCV Library. In O'Reilly Media, 2008.

[22] M. Pereira, V. Santos and P. Dias: Automatic calibration of multiple LIDAR sensors using a moving sphere as target. In Robot 2015: Second Iberian Robotics Conference: Advances in Robotics, vol. 1, pp. 477-486, 2015.

[23] Cerri, Pietro ; Gerelli, Oscar ; Lodi Rizzini, Dario: Bowling for Calibration: An Undemanding Camera Calibration Procedure Using a Sphere. The 5th International Conference on Computer Vision Systems, 2007.

[24] Z.Zhang: A flexible new technique for camera calibration. In IEEE Transactions on Pattern Analysis and Machine Intelligence, vol 22, pp. 1330-1334, 2000.

[25] R. I. Hartley: Theory and practice of projective rectification. In International Journal of Computer Vision, vol 35, pp. 115–127, 1998.

[26] R.Y. Tsai: A versatile camera calibration technique for high-accuracy 3D machine vision metrology using off-the-self TV cameras and lenses. In IEEE Journal of Robotics and Automation, vol 3, pp. 323-344, 1987.

[27] Z.Zhang, P.-S. Tsai, J.E. Cryer and M. Shah: Flexible camera calibration by viewing a plane from unknown orientations. In IEEE International Conference on Computer Vision, vol. 1, pp. 666-673, 1999.

[28] K. Konolige: Small vision system: Hardware and implementation. In Proceedings of the International Symposium on Robotics Research, pp. 111-116, 1997.

[29] H. Hirschmuller: Stereo Processing by Semiglobal Matching and Mutual Information. In IEEE Transactions on Pattern Analysis and Machine Intelligence, vol 30, pp. 328-341, 2008.